nature physics

Article

https://doi.org/10.1038/s41567-022-01853-z

Observation of topological action potentials in engineered tissues

Received: 31 May 2022

Accepted: 17 October 2022

Published online: 22 December 2022

Check for updates

Hillel Ori[1], Marc Duque[1], Rebecca Frank Hayward[2], Colin Scheibner[3], He Tian[1], Gloria Ortiz[4], Vincenzo Vitelli[3] & Adam E. Cohen[1,5]

The interface between two tissues can have very different bioelectrical properties compared to either tissue on its own. Here we show that an interface between non-excitable tissues can be electrically excitable because of an interaction between the currents passing through the gap junctions—electrically resistive intercellular connections—and the non-linear current–voltage dependence in the ion channels on either side of the interface. Our theory shows that this topologically robust excitability occurs over a far larger range of ion channel expression levels than can support excitability in the bulk. The corresponding interfacial action potentials can cause local elevations in calcium concentration, possibly providing a bioelectrical mechanism for interface sensing. The observed topological action potentials point to the possibility of other types of topological effect in electrophysiology and at other diffusively coupled interfaces.

Patterns of membrane potential are thought to play a critical role in many biological patterning processes[1–9]. Less is known about the fate of such patterns when tissues with different resting potential are in contact. In particular, can the interface between two non-excitable tissues be excitable? When cells are gap junction-coupled across the interface, the voltage along a line transverse to the interface must interpolate between steady state voltages of the two halves, including possibly going through unstable or metastable regimes. This continuity requirement on the membrane voltage opens the possibility of robust interfacial action potentials (APs) that would not be supported by the bulk media on either side of the interface.

Robust excitations localized at interfaces are a burgeoning area of basic research and technology[10]. For example, interfacial excitations have been studied in the context of topological insulators spanning electronic[11], photonic[12], mechanical[13–15], hydrodynamic[16] and biochemical reaction–diffusion[17–19] systems. While these systems can often be treated within the topological band theory of linear waves, electrophysiological excitability inherently relies on the topological properties of the underlying non-linear dynamical system.

Historically, spatial structures in bioelectrical signalling have been difficult to investigate experimentally because patch-clamp measurements probed the voltage at only a single point in space. Recent advances in voltage imaging[20,21] opened the door to studying the spatial structures of bioelectrical excitations. By combining patterned optogenetic stimulation and high-speed voltage imaging, one can probe the excitability of a complex tissue as a function of space and time. This approach has been used to identify bioelectrical domain walls in engineered tissues[22] and also to map bioelectrical signals throughout embryonic development[1,20]. Engineered and patterned cells have been a powerful tool for dissecting intercellular molecular signalling cascades[23,24], but despite some theoretical work[25,26], this approach has not previously been applied experimentally to bioelectrical signalling in heterogeneous tissues.

In this Article, we map the excitability at interfaces between non-excitable engineered tissues and observe interface-localized ('topological') APs. Detailed numerical simulations and a simple analytical model capture the key features of these excitations. Our simulations predict that topological APs are exceptionally robust to variations in ion channel levels compared to ordinary APs. These findings suggest a mechanism of bioelectrical signalling that may arise in native tissues and that might be used in engineering synthetic bioelectrical circuits with applications in sensing, tissue engineering and unconventional computation. A theoretical analysis of interfacial APs revealing how their properties stem from topological features of the underlying

[1]Department of Chemistry and Chemical Biology, Harvard University, Cambridge, MA, USA. [2]School of Engineering and Applied Science, Harvard University, Cambridge, MA, USA. [3]James Franck Institute and Department of Physics, University of Chicago, Chicago, IL, USA. [4]Department of Chemistry, University of California, Berkeley, CA, USA. [5]Department of Physics, Harvard University, Cambridge, MA, USA. e-mail: cohen@chemistry.harvard.edu

https://doi.org/10.1038/s41567-022-01853-z

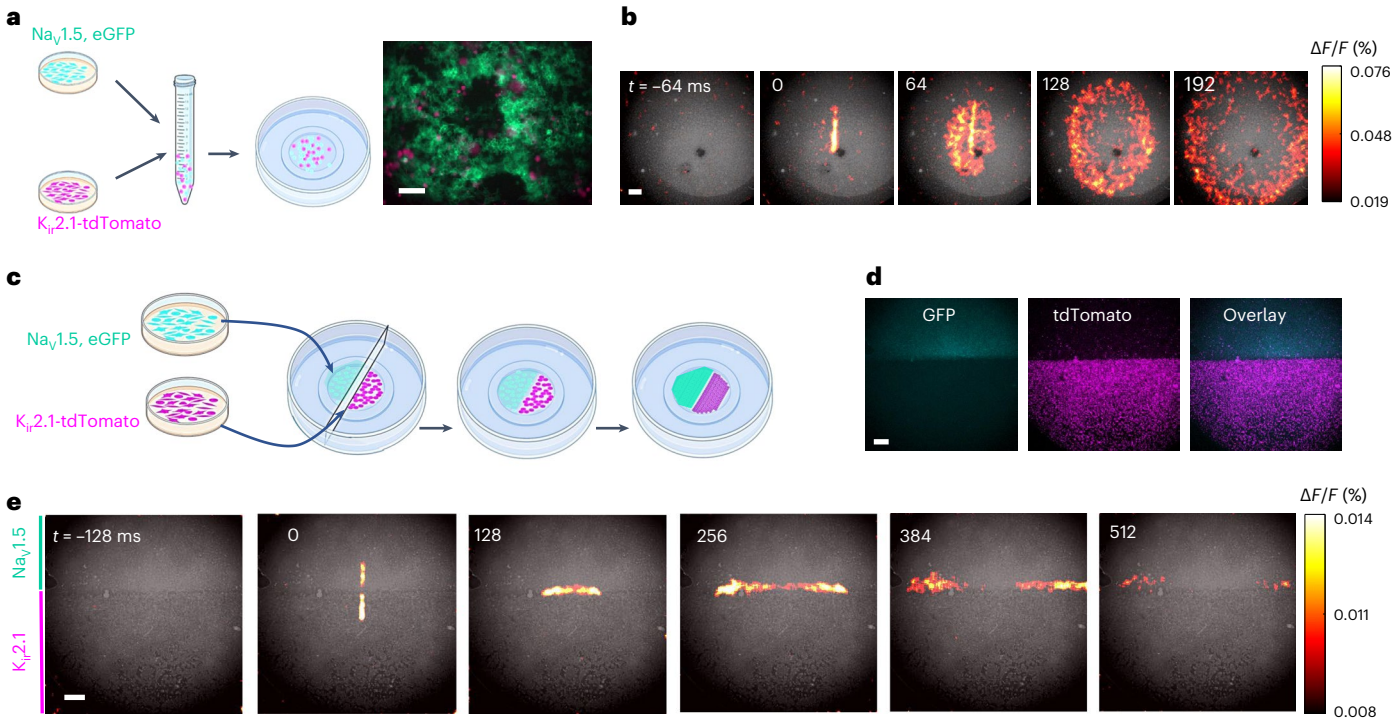

Fig. 1 | Topological APs arise at interfaces of non-excitable tissues. a,**b**, A mixture of non-excitable cells can be excitable. **a**, Left: sample preparation. HEK cells were engineered to express either $K_{ir}2.1$ (an inward-rectifier K^+ channel) or $Na_V1.5$ (a voltage-gated Na^+ channel). All cells also expressed a light-gated ion channel, CheRiff. The two populations were mixed in a 1:1 ratio, plated and grown to form a gap junction-coupled monolayer. Right: distribution of $Na_V1.5$-expressing cells (tagged with a GFP marker) and $K_{ir}2.1$-expressing cells (tagged with a tdTomato marker). Expression is mutually exclusive. **b**, Montage of frames from voltage-imaging video (Supplementary Video 1). The monolayer was stimulated by a short pulse of blue light (vertical bar at $t = 0$). Changes in voltage were then monitored via the fluorescence of the far-red voltage-sensitive dye BeRST1 (baseline signal in grey, $\Delta F/F$ in colour). Optogenetic stimulation evoked outward propagating APs. **c**–**e**, Topological AP at interfaces. **c**, Sample preparation. HEK cells expressing $K_{ir}2.1$ or $Na_V1.5$ were plated on opposite sides of a thin plastic divider. After removal of the divider, the cells migrated to fill the gap and formed a gap junction-coupled interface. **d**, Interface between populations of $Na_V1.5$-expressing cells (tagged with GFP) and $K_{ir}2.1$-expressing cells (tagged with tdTomato). **e**, Montage of frames from a voltage-imaging video (Supplementary Video 2). Optogenetic stimulation spanning the interface at $t = 0$ evoked a topological AP that propagated outwards solely along the interface (baseline signal in grey, $\Delta F/F$ in colour). Scale bars, 0.1 mm (**a**) and 1 mm (**b**, **d** and **e**). See also Extended Data Figs. 1 and 2.

non-linear dynamics (beyond topological band theory) will be presented separately (C.S. et al., manuscript in preparation).

Results

Human embryonic kidney (HEK293) cells become electrically excitable when genetically engineered to express an inward-rectifier potassium channel (for example $K_{ir}2.1$ or $K_{ir}2.3$) and a voltage-gated sodium channel (for example $Na_V1.3$ (ref. [27]), $Na_V1.5$ (ref. [28]) or $Na_V1.7$ (ref. [29])). When grown in a confluent monolayer, endogenous gap junctions introduce nearest-neighbour electrical coupling, which can then support propagating electrical waves. If the cells further express a blue-light-activated cation channel such as CheRiff (ref. [30]) and either express a far-red voltage-indicator protein[21] or are labelled with a red-shifted voltage-sensitive dye[31], then one can optically induce APs and simultaneously map their propagation through the engineered tissue[22,28,32].

First, we explored whether the sodium and potassium channels needed to be in the same cells. We made separate pools of HEK cells that expressed CheRiff and either $Na_V1.5$ alone or $K_{ir}2.1$ alone (Fig. 1a). We mixed the cell populations in a 1:1 ratio and mapped the voltage in confluent monolayer cultures using the far-red voltage-sensitive dye BeRST1 (Methods)[31]. Localized optogenetic stimulation evoked APs that propagated radially outwards (Fig. 1b and Supplementary Video 1). These APs were quantified by the fractional change in fluorescence, $\Delta F/F$, of the BeRST1 indicator. In cultures expressing either $Na_V1.5$ or $K_{ir}2.1$ alone, optical activation of CheRiff did not lead to APs or wave propagation (Extended Data Fig. 1). These results show that a mixture of non-excitable cells can become excitable by sharing currents through gap junctions.

Next, we used a thin plastic divider to physically separate the $Na_V1.5$- and the $K_{ir}2.1$-expressing cells on opposite halves of the culture dish (Fig. 1c and Methods). Fluorescent tags marked the two populations (Fig. 1d). After the cells had settled, we gently removed the divider and let the cells migrate to fill the gap (Methods). This approach led to a clean interface with the two cell populations on opposite sides.

Optogenetic stimulation of either population alone did not evoke APs. Remarkably, optogenetic stimulation with a stripe that spanned the interface induced electrical excitations that propagated along the interfacial line without entering the bulk on either side (Fig. 1e and Supplementary Video 2). The spikes had a width of 0.76 ± 0.15 mm transverse to the interface, a length of 2.21 ± 0.62 mm along the interface and propagated at 12.9 ± 3.5 mm s^{-1} (mean ± s.d., $n = 5$ samples, Fig. 2a). Thus, topological APs can arise between non-excitable tissues. For control experiments, we made interfaces in which one cell population expressed either $Na_V1.5$ or $K_{ir}2.1$, and the adjoining population expressed neither channel. These interfaces were not excitable, confirming the necessity of both ion channels on opposite sides of the interface (Extended Data Fig. 2a,b). Furthermore, in dishes where the $Na_V1.5$- and $K_{ir}2.1$-expressing cells had not yet fully closed the gap, topological APs propagated only in regions where the two cell types had come into contact (Extended Data Fig. 2c).

To better understand our results, we simulated a Hodgkin-Huxley (HH)-like conductance-based model of our experiment using

https://doi.org/10.1038/s41567-022-01853-z

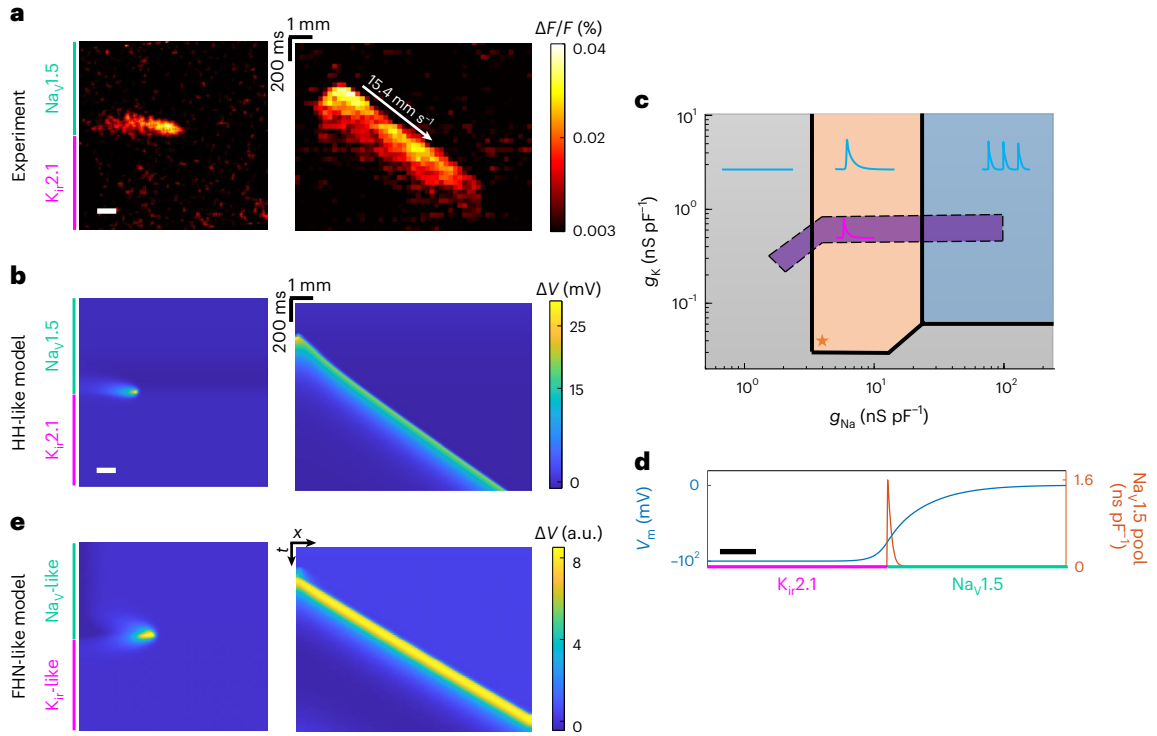

Fig. 2 | Quantification and numerical simulations of topological APs. a, Left: spatial profile of a topological AP. Cyan and magenta lines indicate regions of the sample expressing Na$_V$1.5 and K$_{ir}$2.1, respectively. Scale bar, 1 mm. Right: kymograph constructed by averaging transverse to the interface, showing topological AP propagation. **b**, Numerical simulations of an interface between a K$_{ir}$2.1-expressing cell population (g_K = 0.04 nS pF^{-1}, E_K = −107 mV) and a Na$_V$1.5-expressing cell population (g_{Na} = 3.9 nS pF^{-1}, E_{Na} = 75 mV). Left: image of a topological AP propagating along a tissue interface (Supplementary Video 3). Scale bar, 1 mm. Right: kymograph showing topological AP propagation. The colour scale corresponds to deviation from local resting potential. **c**, Calculated phase diagram of excitability of K$_{ir}$2.1–Na$_V$1.5 interface. The parameter space is divided into non-excitable, excitable, and spontaneously active phases, indicated by representative activity patterns (blue lines). The purple region indicates the excitable phase of a homogenous system, where each cell expresses both Na$_V$1.5 and K$_{ir}$2.1 channels. The interfacial system has a spontaneously active phase (blue region) that is absent in the homogenous system. The orange star corresponds to the parameters used for the simulations in **b**. **d**, Steady-state resting voltage and sodium channel availability along a line transverse to the interface. The voltage varies continuously between a polarized state on the K$_{ir}$2.1 side and a depolarized state on the Na$_V$1.5 side. The available reserve of Na$_V$1.5 conductance ($g_{Na} \times (1 - m^3)\, h$) has a peak near the interface. The variables m and h are the sodium channel activation and inactivation gates, respectively, defined in Supplementary Model 1. The band of high Na$_V$1.5 reserve supports AP propagation. Scale bar, 0.2 mm. **e**, Numerical simulation of a simplified FHN-like model of topological APs (See Supplementary Model 2 for details.). Left: image of a topological AP propagating along a tissue interface. Right: kymograph showing topological AP propagation. Scale bars omitted because space and time units are arbitrary. Voltage scale, ΔV, is in arbitrary units (a.u.). See also Extended Data Figs. 3–5.

established parameters for K$_{ir}$2.1 and Na$_V$1.5 (refs. [22,33]) (Supplementary Model 1). This model reproduced the basic phenomena, showing interface-localized AP initiation and propagation (Fig. 2b and Supplementary Video 3). We then simulated the effect of changes in the expression level of the gap junctions, Na$_V$1.5, or K$_{ir}$2.1. Modulating the gap junction conductance, G_{gj}, changed the width, length and conduction speed of the topological AP, with all three parameters scaling as $(G_{gj})^{1/2}$, as one would expect from dimensional analysis (Extended Data Fig. 3). Topological APs arose over at least a 60-fold variation in g_{Na} and at least a 1,000-fold variation in g_K, persisting to the highest levels of g_K and g_{Na} simulated (Fig. 2c).

We then performed analogous simulations where the Na$_V$1.5 and K$_{ir}$2.1 were homogeneously distributed through all cells. For cells co-expressing both ion channels, excitability occurred over a much narrower range of expression levels (~30-fold in Na$_V$1.5 but only ~3-fold in K$_{ir}$2.1; Fig. 2c). This observation highlights an important difference between an interface and a homogeneous mixture of the two types of cell. In the homogeneous case, excitability required a delicate balance of depolarizing (Na$_V$, leak, channelrhodopsin) and polarizing (K$_{ir}$) currents to drive all the phases of the AP (refs. [34,35]). In the interfacial structure, the gap junction coupling created an effective weighted average between the Na$_V$ and K$_{ir}$ currents, whose weights depended on the distance from the interface (Fig. 2d). Thus, spatial separation of the Na$_V$ and the K$_{ir}$ components, paradoxically, led to a system where the excitability was far more robust than in the system where these two components were mixed.

To facilitate an understanding of the basic requirements for topological APs, we developed a simplified model inspired by the FitzHugh–Nagumo (FHN) model (Supplementary Model 2 and Supplementary Code)[36,37]. We broke the characteristic N-shaped non-linearity of the FHN model into two components: a non-linear component approximating the shape of a Na$_V$ current–voltage (I–V) curve and a linear component mimicking the restoring nature of the K$_{ir}$ current. Each component was active in only one half-space. Neither component alone supported AP generation because each had a single zero-crossing and hence a single stable resting potential. However, at the interface, the I–V curve had contributions from both the Na$_V$-like and the K$_{ir}$-like components and had three zero crossings and hence could support non-linear excitations (Extended Data Fig. 4). The simplified FHN-like model reproduced our observed propagating topological APs (Fig. 2e). The model supports all three excitability states (quiescence, stimulus-triggered APs and spontaneous oscillations) shown by the HH-like model (compare Extended Data Fig. 5 to Fig. 2c). These observations suggest that tissue interfaces might support a rich repertoire of novel bioelectrical phenomena.

https://doi.org/10.1038/s41567-022-01853-z

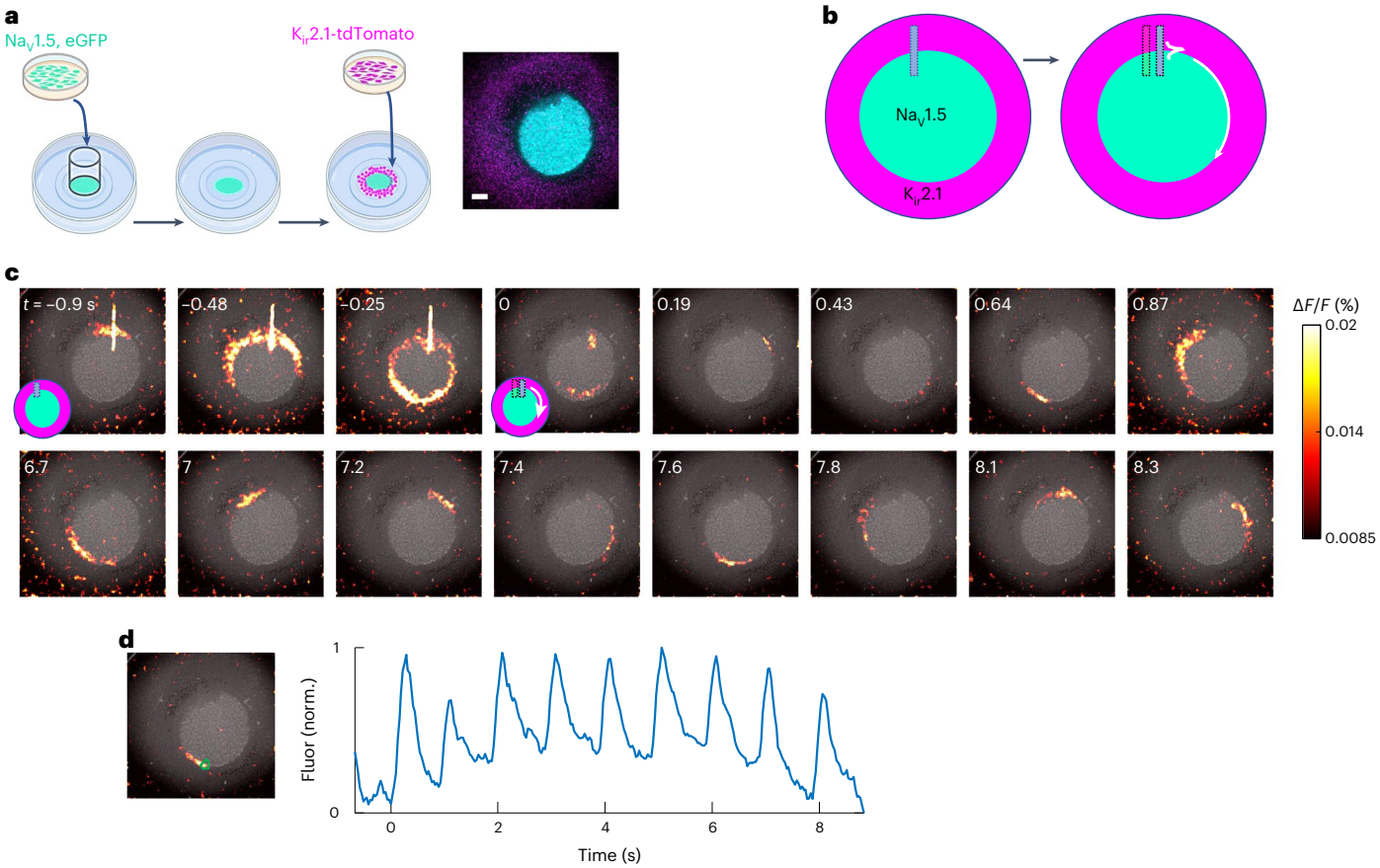

Fig. 3 | Persistently propagating topological APs at a circular interface. a, Sample preparation. HEK cells expressing $Na_V1.5$ and CheRiff were seeded into the circular region defined by a thin plastic cylinder. HEK cells expressing $K_{ir}2.1$ and CheRiff were then added and settled in the unoccupied periphery. Image at the right shows $Na_V1.5$-expressing cells (cyan) and $K_{ir}2.1$-expressing cells (magenta). **b**, Stimulation protocol for evoking a unidirectional topological AP wave. A long (450 ms) illumination pulse was delivered to a portion of the interface, to drive local $Na_V1.5$ inactivation. A short (30 ms) pulse was then delivered to a nearby interface region, evoking a topological AP that propagated unidirectionally. By the time the AP had completed one cycle, the inactivated Na_V channels had recovered, permitting cyclical propagation. **c**, Montage showing application of the inactivation stimulus, the trigger stimulus and persistent AP propagation along the interface. **d**, Time-dependent fluorescence in the region indicated by the green polygon, showing a persistently propagating topological AP. Scale bar, 1 mm. Panels **c** and **d** show same field of view as **a**. See also Extended Data Fig. 6 and Supplementary Video 4.

We then explored experimentally the interaction of interface topology and sample topology. Using a plastic drinking straw as a separator, we plated $Na_V1.5$-expressing cells in a disc and $K_{ir}2.1$-expressing cells in the surrounding region (Fig. 3 and Methods). We then removed the straw and let the cells form a circular interface. Optical stimulation in a line across the interface evoked topological APs that propagated bidirectionally around the interface, annihilating each other when they collided. To evoke a directional wave, we applied a tonic stimulation with a line to create a thin zone of Na_V channel inactivation. We then turned off the tonic stimulation and stimulated one side of this zone briefly. This stimulus protocol created an AP propagating in only one direction. The inactivated Na_V channels recovered by the time the AP had completed one trip around the disc. Thereafter the AP propagated around the interface, circulating stably for many minutes (Extended Data Fig. 6 and Supplementary Video 4). These results demonstrate that topological APs can sense the topology of tissue boundaries and can store information via their handedness of circulation whose sign is set by initial conditions.

In the presence of voltage-gated Ca^{2+} channels, topological APs might lead to locally elevated Ca^{2+}, which could then turn on downstream patterns of gene expression. First, we tested whether co-expression of a T-type calcium channel, $Ca_V3.2$, and $K_{ir}2.3$ in HEK cells were sufficient, on their own, to support AP propagation. We used HEK cells with constitutive expression of $K_{ir}2.3$, doxycycline-inducible expression of $Ca_V3.2$ (ref. [38]) and lentiviral expression of CheRiff for optogenetic stimulation. We induced $Ca_V3.2$ expression with doxycycline and then mapped the voltage in confluent monolayer cultures of these cells (Extended Data Fig. 7a). Local optogenetic stimulation induced APs that propagated radially outwards and then broke up into self-sustaining spiral waves (Supplementary Video 5). Nifedipine is primarily known as an L-type calcium channel blocker, but at high concentrations (>22 μM) nifedipine blocks T-type channels such as $Ca_V3.2$ as well[39]. Incubation with nifedipine (50 μM) abolished the excitability (Extended Data Fig. 7b). Samples where $Ca_V3.2$ expression was not induced were also not excitable (Extended Data Fig. 7c). Together, these results establish that $Ca_V3.2$ and $K_{ir}2.3$ are sufficient to sustain propagating APs in confluent HEK cell monolayers.

We then asked whether topological APs could arise at the interface between cells expressing $Ca_V3.2$ and cells expressing $K_{ir}2.1$. As with the Na_V channels, optogenetic stimulation with a stripe that spanned the interface induced excitations in membrane voltage that propagated along the interface (Fig. 4a and Supplementary Video 6). In separate samples, we used a far-red calcium-sensitive dye (Methods) and observed propagating Ca^{2+} signals along the interface too (Fig. 4b and Supplementary Video 7). These results show that topological APs can be driven by multiple types of depolarizing channel (Na_V, Ca_V) and can drive increases in intracellular Ca^{2+} in cells within an electrical coupling length of a tissue interface.

https://doi.org/10.1038/s41567-022-01853-z

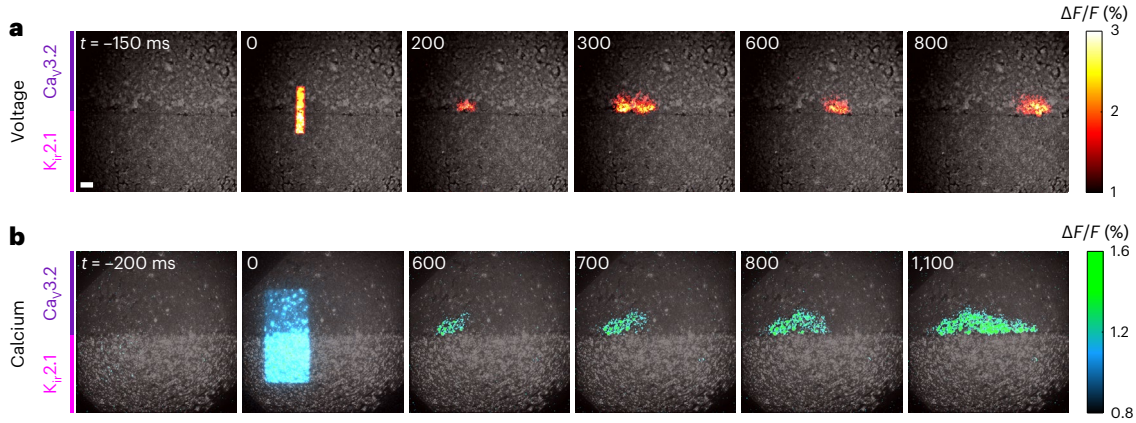

Fig. 4 | Topological APs driven by Ca^{2+} currents. a, Montage of frames from a voltage-imaging video (Supplementary Video 6). Optogenetic stimulation spanning the interface at $t = 0$ evoked a topological AP that propagated outwards solely along the interface. **b**, Montage of frames from a calcium-imaging video (from a different sample, Supplementary Video 7). Optogenetic stimulation at the interface evoked a calcium signal that propagated along the interface. Scale bar, 1 mm. Field of view in **b** is the same size as in **a**. Baseline signal in grey, $\Delta F/F$ in colour. See also Extended Data Fig. 7.

Discussion

The non-linear behaviour of ion channels, together with gap junctional sharing of currents, gives tissue interfaces unique excitability properties that are different from those of the bulk. In this Article, we have shown that: (1) mixtures of non-excitable cells can be excitable, (2) an interface between non-excitable tissues can be excitable, (3) topological APs at tissue interfaces are far more robust to variations in ion channel expression than are APs in homogeneous tissues, (4) a circular tissue interface can support stably circulating topological APs and (5) topological APs can drive local elevations in Ca^{2+} concentration.

It is useful to compare the observed excitable interfaces to the phenomenology of edge modes in topological insulators[10]. The two effects are analogous in the following sense: topological insulators host a conducting boundary at the interface between two distinct bulk insulators. Likewise, the topological APs are excitations at the interface between two tissues that alone are not excitable. However, the theory of edge modes can be often formulated within topological band theory: the amplitude of the relevant waves is proportional to the amplitude of the drive and the waves obey the superposition principle. For the excitable interfaces studied in this Article, the modes are either self-exciting or require a finite amplitude perturbation and they do not obey a superposition principle because of a finite refractory period. Non-linear topological excitations have been studied in a mechanical context[40], but not previously, to our knowledge, in the context of bioelectricity.

To see intuitively how an interface enables excitability, first note that for a single cell (or a homogeneous tissue) to be excitable, the ratio of the conductances of the two channels g_{Na}/g_K must be neither too small nor too large: the sodium current must overwhelm the potassium current on the upstroke, but the potassium current must overwhelm the sodium current on the downstroke. When the cells are gap junction coupled, the ionic currents introduce an averaging effect since each cell seeks to match the mean voltage of its neighbours. A cell that contains only one type of ion channel is nonetheless influenced by the other type of current, which spreads along the chain of gap junction couplings transverse to the interface. In the presence of an interface between pure Na_V and pure K_{ir} conductances, one can always find an averaging window with a ratio of sodium to potassium currents conducive to excitability. However, simply having an interface is not always sufficient (even though the averaging will occur). In multicellular models, the interface plays a crucial role in controlling topological features of the dynamical system, such as the number of fixed points and their Morse indexes that ultimately decide the fate and nature of interfacial excitability. A detailed topological analysis of excitable interfaces is in preparation (C.S. et al., manuscript in preparation).

The existence of topological APs at tissue interfaces raises the possibility of other types of topological effect in electrophysiology. For instance, our numerical simulations predicted a regime in which a $Na_V1.5$–$K_{ir}2.1$ interface shows pacemaking activity, whereas homogeneous monolayers of cells co-expressing $Na_V1.5$ and $K_{ir}2.1$ do not show pacemaking activity under any conditions. In the interfacial case, the membrane voltage can transition through a region where there is no stable fixed point for the voltage. By contrast, in the homogeneous case, there is always a global fixed point near either the K^+ or Na^+ reversal potential. This explains the absence of pacemaking activity. Other combinations of ion channels could lead to additional topological effects. For instance, expression of pacemaker channels on one side of the interface might lead to spontaneous spiking that starts only when two tissues touch, providing a means to signal first contact. Depending on the other ion channels on both sides of the interface, these contact-evoked spikes could either propagate just along the interface, into the bulk on one side or into the bulk on both sides. Topological electrophysiology mechanisms could enable cells to sense the presence of nearby tissue interfaces, to determine the topology of their tissue environment or to communicate over long distances.

The ways in which bioelectrical signals complement chemical signals in embryonic development, morphogenesis and wound healing[1,5,8,9,41,42] are still being worked out. It is not yet known whether topological excitations arise in native tissues. Recent work has highlighted the importance of voltage-gated Ca^{2+} channels in development[43–45]. These effects occur in nominally non-excitable cells. However, our results highlight that excitability need not be an intrinsic feature of a cell. Instead, it can emerge as a collective property of the whole tissue. Interactions between zebrafish skin melanophores and xanthophores also suggest a contact-dependent bioelectrical signalling mechanism[46]. Our results suggest that analyses of such effects should not just examine the properties of individual cell types, but should also consider tissue interfaces as distinct electrophysiological entities. Finally, we note that due to the parallel structure of the Hodgkin–Huxley and Turing reaction–diffusion equations, analogous interfacial excitations could also occur in chemical reaction–diffusion systems. More broadly, we suggest that interfacial excitations merit study as distinct entities in spatially extended active matter[47] and other non-linear dynamical systems, ranging from ecology to epidemiology.

Online content

Any methods, additional references, Nature Portfolio reporting summaries, source data, extended data, supplementary information, acknowledgements, peer review information; details of author contributions and competing interests; and statements of data and code availability are available at https://doi.org/10.1038/s41567-022-01853-z.

References

1. Levin, M. Bioelectric signaling: Reprogrammable circuits underlying embryogenesis, regeneration, and cancer. *Cell* **184**, 1971–1989 (2021).
2. Pietak, A. & Levin, M. Bioelectric gene and reaction networks: computational modelling of genetic, biochemical and bioelectrical dynamics in pattern regulation. *J. R. Soc. Interface* **14**, 20170425 (2017).
3. Levin, M. Endogenous bioelectrical networks store non-genetic patterning information during development and regeneration. *J. Physiol.* **592**, 2295–2305 (2014).
4. Levin, M. Bioelectric mechanisms in regeneration: unique aspects and future perspectives. *Semin. Cell Dev. Biol.* **20**, 543–556 (2009).
5. Tyler, S. E. B. Nature's electric potential: a systematic review of the role of bioelectricity in wound healing and regenerative processes in animals, humans, and plants. *Front. Physiol.* **8**, 627 (2017).
6. Cervera, J., Alcaraz, A. & Mafe, S. Bioelectrical signals and ion channels in the modeling of multicellular patterns and cancer biophysics. *Sci. Rep.* **6**, 20403 (2016).
7. Payne, S. L., Levin, M. & Oudin, M. J. Bioelectric control of metastasis in solid tumors. *Bioelectricity* **1**, 114–130 (2019).
8. Robinson, K. R. & Messerli, M. A. Left/right, up/down: The role of endogenous electrical fields as directional signals in development, repair and invasion. *BioEssays* **25**, 759–766 (2003).
9. Reid, B. & Zhao, M. The electrical response to injury: molecular mechanisms and wound healing. *Adv. Wound Care* https://doi.org/10.1089/wound.2013.0442 (2014).
10. Hasan, M. Z. & Kane, C. L. Colloquium: topological insulators. *Rev. Mod. Phys.* **82**, 3045–3067 (2010).
11. Vergniory, M. G. et al. A complete catalogue of high-quality topological materials. *Nature* **566**, 480–485 (2019).
12. Haldane, F. D. M. & Raghu, S. Possible realization of directional optical waveguides in photonic crystals with broken time-reversal symmetry. *Phys. Rev. Lett.* **100**, 013904 (2008).
13. Süsstrunk, R. & Huber, S. D. Observation of phononic helical edge states in a mechanical topological insulator. *Science* **349**, 47–50 (2015).
14. Nash, L. M. et al. Topological mechanics of gyroscopic metamaterials. *Proc. Natl Acad. Sci. USA* **112**, 14495–14500 (2015).
15. Paulose, J., Chen, B. G. & Vitelli, V. Topological modes bound to dislocations in mechanical metamaterials. *Nat. Phys.* **11**, 153–156 (2015).
16. Souslov, A., Dasbiswas, K., Fruchart, M., Vaikuntanathan, S. & Vitelli, V. Topological waves in fluids with odd viscosity. *Phys. Rev. Lett.* **122**, 128001 (2019).
17. Gong, Z. et al. Topological phases of non-Hermitian systems. *Phys. Rev. X* **8**, 031079 (2018).
18. Dasbiswas, K., Mandadapu, K. K. & Vaikuntanathan, S. Topological localization in out-of-equilibrium dissipative systems. *Proc. Natl Acad. Sci. USA* **115**, E9031–E9040 (2018).
19. Murugan, A. & Vaikuntanathan, S. Topologically protected modes in non-equilibrium stochastic systems. *Nat. Commun.* **8**, 13881 (2017).
20. Hou, J. H., Kralj, J. M., Douglass, A. D., Engert, F. & Cohen, A. E. Simultaneous mapping of membrane voltage and calcium in zebrafish heart *in vivo* reveals chamber-specific developmental transitions in ionic currents. *Front. Physiol.* **5**, 344 (2014).
21. Adam, Y. et al. Voltage imaging and optogenetics reveal behaviour-dependent changes in hippocampal dynamics. *Nature* **569**, 413 (2019).
22. McNamara, H. M. et al. Bioelectrical domain walls in homogeneous tissues. *Nat. Phys.* **16**, 357–364 (2020).
23. Ma, Y. et al. Synthetic mammalian signaling circuits for robust cell population control. *Cell* **185**, 967–979 (2022).
24. Warmflash, A., Sorre, B., Etoc, F., Siggia, E. D. & Brivanlou, A. H. A method to recapitulate early embryonic spatial patterning in human embryonic stem cells. *Nat. Methods* **11**, 847–854 (2014).
25. Cervera, J., Levin, M. & Mafe, S. Bioelectrical coupling of single-cell states in multicellular systems. *J. Phys. Chem. Lett.* **11**, 3234–3241 (2020).
26. Xu, J. et al. The role of cellular coupling in the spontaneous generation of electrical activity in uterine tissue. *PLoS One* **10**, e0118443 (2015).
27. Park, J. et al. Screening fluorescent voltage indicators with spontaneously spiking HEK cells. *PLoS One* **8**, e85221 (2013).
28. McNamara, H. M., Zhang, H., Werley, C. A. & Cohen, A. E. Optically controlled oscillators in an engineered bioelectric tissue. *Phys. Rev. X* **6**, 031001 (2016).
29. Zhang, H., Reichert, E. & Cohen, A. E. Optical electrophysiology for probing function and pharmacology of voltage-gated ion channels. *eLife* **5**, e15202 (2016).
30. Hochbaum, D. R. et al. All-optical electrophysiology in mammalian neurons using engineered microbial rhodopsins. *Nat. Methods* **11**, 825–833 (2014).
31. Huang, Y. L., Walker, A. S. & Miller, E. W. A photostable silicon rhodamine platform for optical voltage sensing. *J. Am. Chem. Soc.* **137**, 10767–10776 (2015).
32. McNamara, H. M. et al. Geometry-dependent arrhythmias in electrically excitable tissues. *Cell Syst.* **7**, 359–370.e6 (2018).
33. ten Tusscher, K. H. W. J., Noble, D., Noble, P. J. & Panfilov, A. V. A model for human ventricular tissue. *Am. J. Physiol. Heart Circ. Physiol.* **286**, H1573–H1589 (2004).
34. Ori, H., Marder, E. & Marom, S. Cellular function given parametric variation in the Hodgkin and Huxley model of excitability. *Proc. Natl Acad. Sci. USA* **115**, E8211–E8218 (2018).
35. Ori, H., Hazan, H., Marder, E. & Marom, S. Dynamic clamp constructed phase diagram for the Hodgkin and Huxley model of excitability. *Proc. Natl Acad. Sci. USA* **117**, 3575–3582 (2020).
36. FitzHugh, R. Impulses and physiological states in theoretical models of nerve membrane. *Biophys. J.* **1**, 445–466 (1961).
37. Nagumo, J., Arimoto, S. & Yoshizawa, S. An active pulse transmission line simulating nerve axon. *Proc. IRE* **50**, 2061–2070 (1962).
38. Belardetti, F. et al. A fluorescence-based high-throughput screening assay for the identification of T-type calcium channel blockers. *Assay Drug Dev. Technol.* **7**, 266–280 (2009).
39. Perez-Reyes, E., Van Deusen, A. L. & Vitko, I. Molecular pharmacology of human $Ca_V3.2$ T-type Ca^{2+} channels: block by antihypertensives, antiarrhythmics, and their analogs. *J. Pharmacol. Exp. Ther.* **328**, 621–627 (2009).
40. Chen, B. G., Upadhyaya, N. & Vitelli, V. Nonlinear conduction via solitons in a topological mechanical insulator. *Proc. Natl Acad. Sci. USA* **111**, 13004–13009 (2014).
41. Gregor, T., Tank, D. W., Wieschaus, E. F. & Bialek, W. Probing the limits to positional information. *Cell* **130**, 153–164 (2007).
42. Braun, E. & Ori, H. Electric-induced reversal of morphogenesis in *Hydra*. *Biophys. J.* **117**, 1514–1523 (2019).
43. Pitt, G. S., Matsui, M. & Cao, C. Voltage-gated calcium channels in nonexcitable tissues. *Annu. Rev. Physiol.* **83**, 183–203 (2021).
44. Atsuta, Y., Tomizawa, R. R., Levin, M. & Tabin, C. J. L-type voltage-gated Ca^{2+} channel $Ca_V1.2$ regulates chondrogenesis

during limb development. *Proc. Natl Acad. Sci. USA* **116**, 21592–21601 (2019).
45. Lin, S.-S. et al. $Ca_v3.2$ T-type calcium channel is required for the NFAT-dependent Sox9 expression in tracheal cartilage. *Proc. Natl Acad. Sci. USA* **111**, E1990–E1998 (2014).
46. Inaba, M., Yamanaka, H. & Kondo, S. Pigment pattern formation by contact-dependent depolarization. *Science* **335**, 677 (2012).
47. Shankar, S., Souslov, A., Bowick, M. J., Marchetti, M. C. & Vitelli, V. Topological active matter. *Nat. Rev. Phys.* **4**, 380–398 (2022).

Publisher's note Springer Nature remains neutral with regard to jurisdictional claims in published maps and institutional affiliations.

Springer Nature or its licensor (e.g. a society or other partner) holds exclusive rights to this article under a publishing agreement with the author(s) or other rightsholder(s); author self-archiving of the accepted manuscript version of this article is solely governed by the terms of such publishing agreement and applicable law.

© The Author(s), under exclusive licence to Springer Nature Limited 2022

Methods

Cell line generation and culture

Cells stably co-expressing $Na_V1.5$ and CheRiff-eGFP are described in ref. [29]. For cells expressing $K_{ir}2.1$ and CheRiff, cells constitutively expressing CheRiff were transiently transfected with pCAG-$K_{ir}2.1$-T2A-tdTomato (from Massimo Scanziani, Addgene 60598) using CalFectin transfection reagent (SignaGen Laboratories) following the manufacturer's directions. Cells were seeded in imaging plates 24–48 h after transfection. HEK cells were maintained in Dulbecco's modified Eagle medium with 10% fetal bovine serum (DMEM-10), penicillin (100 U ml^{-1}) and streptomycin (100 mg ml^{-1}). Cells stably expressing human $Ca_V3.2$, along with cells constitutively expressing $K_{ir}2.3$ and doxycycline-inducible $Ca_V3.2$, were a generous gift from T. Snutch and are described in ref. [38]. These cells were infected with a lentiviral vector expressing pCMV-CheRiff-CFP (Addgene 136636) to render them light sensitive.

Sample preparation

Dishes (35 mm) with 14 mm glass coverslip bottoms (Cellvis, #D35-14-1.5-N) were coated with polyethylenimine (PEI). Two days prior to imaging, linear interfaces were created by seeding $Na_V1.5$- and $K_{ir}2.1$-expressing cells separated by a 100 µm-thick plastic divider, 4×10^5 cells of each type. After 2 h, the divider was carefully removed, the plate was gently washed with phosphate-buffered saline (PBS) to remove unattached cells and the plate was incubated in culture medium. For the circular interfaces, the central island was created by seeding 5×10^5 $Na_V1.5$-expressing cells inside a region defined by a circular 5 mm-diameter plastic cylinder (a cut drinking straw). After 2 h, the cylinder was removed, unattached cells were removed by gentle washing with PBS and the plate was incubated overnight with culture medium. Approximately 10^6 $K_{ir}2.1$-expressing cells were then seeded onto the dish. The $K_{ir}2.1$ cells were primarily attached in the annular region not already occupied by $Na_V1.5$-expressing cells.

Imaging and stimulation

For voltage imaging, cells were washed to remove culture medium and then incubated with 1–2 µM BeRST1 dye in PBS for 30 min in a tissue culture incubator. Immediately before imaging, samples were washed twice and immersed in imaging solution containing 125 mM NaCl, 15 mM HEPES, 25 mM glucose, 2.5 mM KCl, 1 mM $MgCl_2$ and 2 mM $CaCl_2$ with the pH adjusted to 7.3 with NaOH. Sample preparation for Ca^{2+} imaging was similar, except that the cells were washed and incubated with 3 µM BioTracker 609 Red Ca^{2+} AM Dye (EMD Millipore #SCT021) in PBS for 30 min in a tissue culture incubator, then washed and immersed in imaging solution. Widefield imaging was performed using an Axiovert 200 (Zeiss) inverted microscope equipped with a light source (xenon arc, XBO 75 W) and filter sets for the GFP, tdTomato, BeRST1 and calcium dye channels. Light was collected using a 2×, numerical aperture 0.1 objective lens (ThorLabs #TL2X-SAP) into an electron-multiplying charged-coupled device camera (Andor iXon EM+ 897, 512 × 512 pixels, 35 frames per s). The field of view (FOV) was expanded to 9.9 mm in the sample plane by placing a 0.5× image reducer (View Solutions, #MA513302) in the light collection path. CheRiff was excited by a 470 nm light-emitting diode (LED) (ThorLabs #M470L4-C4) connected to the topside illumination path. The stimulation region was defined by a thin slit inserted in the excitation beam and projected onto the sample plane by the microscope condenser. The camera was controlled using the Andor SOLIS software. The LED illumination was controlled by a National Instruments DAQ card. The camera and LED were synchronized using a custom MATLAB code. For imaging and patterned optogenetic stimulation of $Ca_V3.2$–$K_{ir}2.3$ monolayers and $Ca_V3.2$–$K_{ir}2.1$ interfaces we used an ultrawidefield microscope as described in ref. [48].

Data analysis

All data were processed and analysed using custom software (MATLAB). The baseline fluorescence, F, of the BeRST1 signal was calculated for each pixel from the mean intensity over the time series. The video was then converted into units of $\Delta F/F$ and smoothed by spatially filtering with a 12 × 12 pixels kernel.

For the linear interface experiments (Fig. 1), ten consecutive trials were averaged before converting to $\Delta F/F$ units. To calculate the spatial shape of the propagating AP (Fig. 2a), images acquired at different times were laterally shifted to cancel the motion of the AP wavefront. Background noise from variation between rows was suppressed by setting pixels below the 20th percentile of their row to the minimum intensity of the frame. Finally, the video was averaged along the time axis with a 12-frames window.

Kymographs were constructed by averaging rectangles of 40 × 10 pixels along the interface.

For the circular interface experiment (Fig. 3) the time series of the $\Delta F/F$ video was reconstructed from a detrended vectorized $\Delta F/F$ sequence to account for changes in baseline signal due to photobleaching. In addition to spatial filtering, videos were averaged along time with a six-frame sliding window. For the time-trace plot (Fig. 3d) a spatial region of interest was defined and averaged across pixels.

GFP and tdTomato images (Fig. 1a,b) were processed by subtracting a background image (no illumination) and dividing pixel-wise by a reference image (a dish with no cells) to account for spatial variations in illumination intensity. A gamma correction was applied to the tdTomato image to permit visualization of cells with widely varying expression levels.

Numerical modelling

Model equations and simulation methods can be found in Supplementary Models 1 and 2 and Supplementary Code.

Reporting summary

Further information on research design is available in the Nature Portfolio Reporting Summary linked to this article.

Data availability

Source data are available for this paper. All other data that support the plots within this paper and other findings of this study are available from the corresponding author upon reasonable request.

Code availability

Computer code for simulations of Supplementary Model 2 is provided in Supplementary Code. Computer codes for Supplementary Model 1 and for data analysis are available from the authors upon reasonable request.

References

48. Werley, C. A., Chien, M.-P. & Cohen, A. E. Ultrawidefield microscope for high-speed fluorescence imaging and targeted optogenetic stimulation. *Biomed. Opt. Express* **8**, 5794–5813 (2017).

Acknowledgements

This work was supported by the Vannevar Bush Faculty Fellowship grant N00014-18-1-2859 (A.E.C.), National Science Foundation QuBBE QLCI grant OMA-2121044 (A.E.C.), an EMBO Fellowship ALTF 543-2020 (H.O.), a Bloomenthal Fellowship (C.S.), the National Science Foundation Graduate Research Fellowship grant 1746045 (C.S.), the Simons Foundation (V.V.), the Complex Dynamics and Systems Program of the Army Research Office grant W911NF-19-1-0268 (V.V.) and the National Science Foundation grant DMR-2118415 (V.V.). We thank N. Ziv and his laboratory for hosting H.O. during the COVID-19 pandemic. We thank T. Snutch for helpful discussions and for providing cells expressing $Ca_V3.2$ and $K_{ir}2.3$. We thank E. Miller for the BeRST1 dye. We thank S. Xu for helpful discussions. We thank S. Begum, A. Preecha, T. Galateanu and L. Odessky for technical assistance.

Author contributions

H.O. and A.E.C. conceived and designed the study and developed the FHN-inspired model. H.O. conducted the experiments and simulations and analysed results with assistance from M.D. C.S. and V.V. defined the topological interpretation. R.F.H. and H.T. assisted with method development and cell line engineering. G.O. provided BeRST1 dye reagent. A.E.C., H.O., C.S. and V.V. wrote the manuscript.

Competing interests

The authors declare no competing interests.

Additional information

Extended data is available for this paper at https://doi.org/10.1038/s41567-022-01853-z.

Supplementary information The online version contains supplementary material available at https://doi.org/10.1038/s41567-022-01853-z.

Correspondence and requests for materials should be addressed to Adam E. Cohen.

Peer review information *Nature Physics* thanks Min Zhao, Chike Cao and the other, anonymous, reviewer(s) for their contribution to the peer review of this work.

Reprints and permissions information is available at www.nature.com/reprints.

https://doi.org/10.1038/s41567-022-01853-z

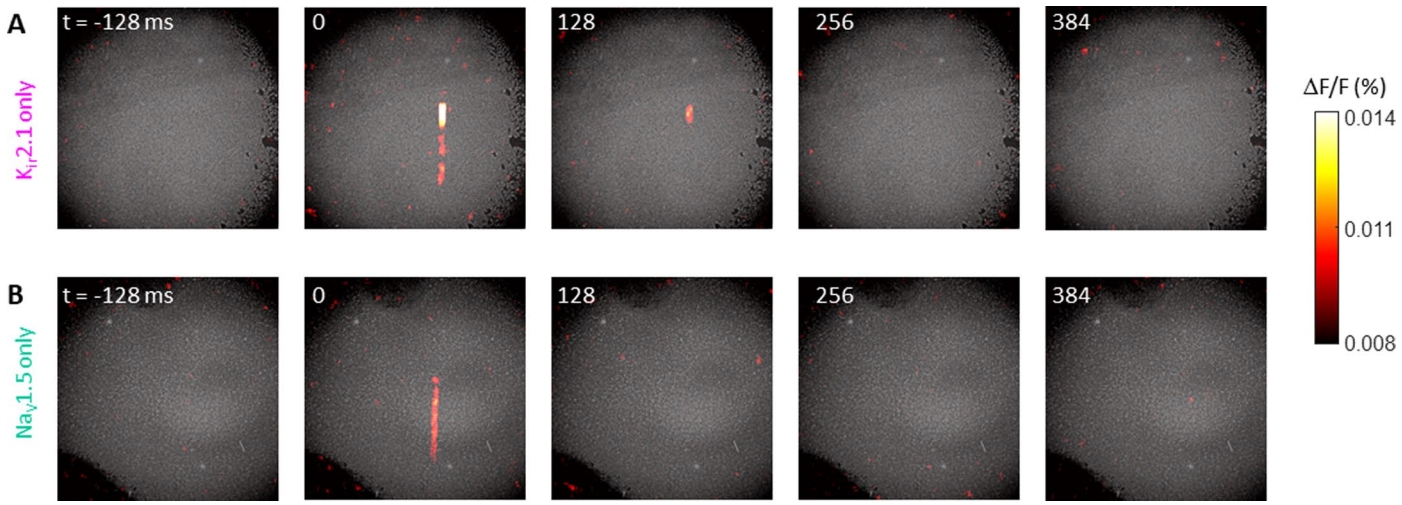

Extended Data Fig. 1 | Control experiments showing absence of excitability in cells expressing only one voltage-dependent channel. In both panels, the cells also expressed a channelrhodopsin, CheRiff. The stimulus was delivered as a bar of blue light at $t = 0$. Related to Fig. 1.

https://doi.org/10.1038/s41567-022-01853-z

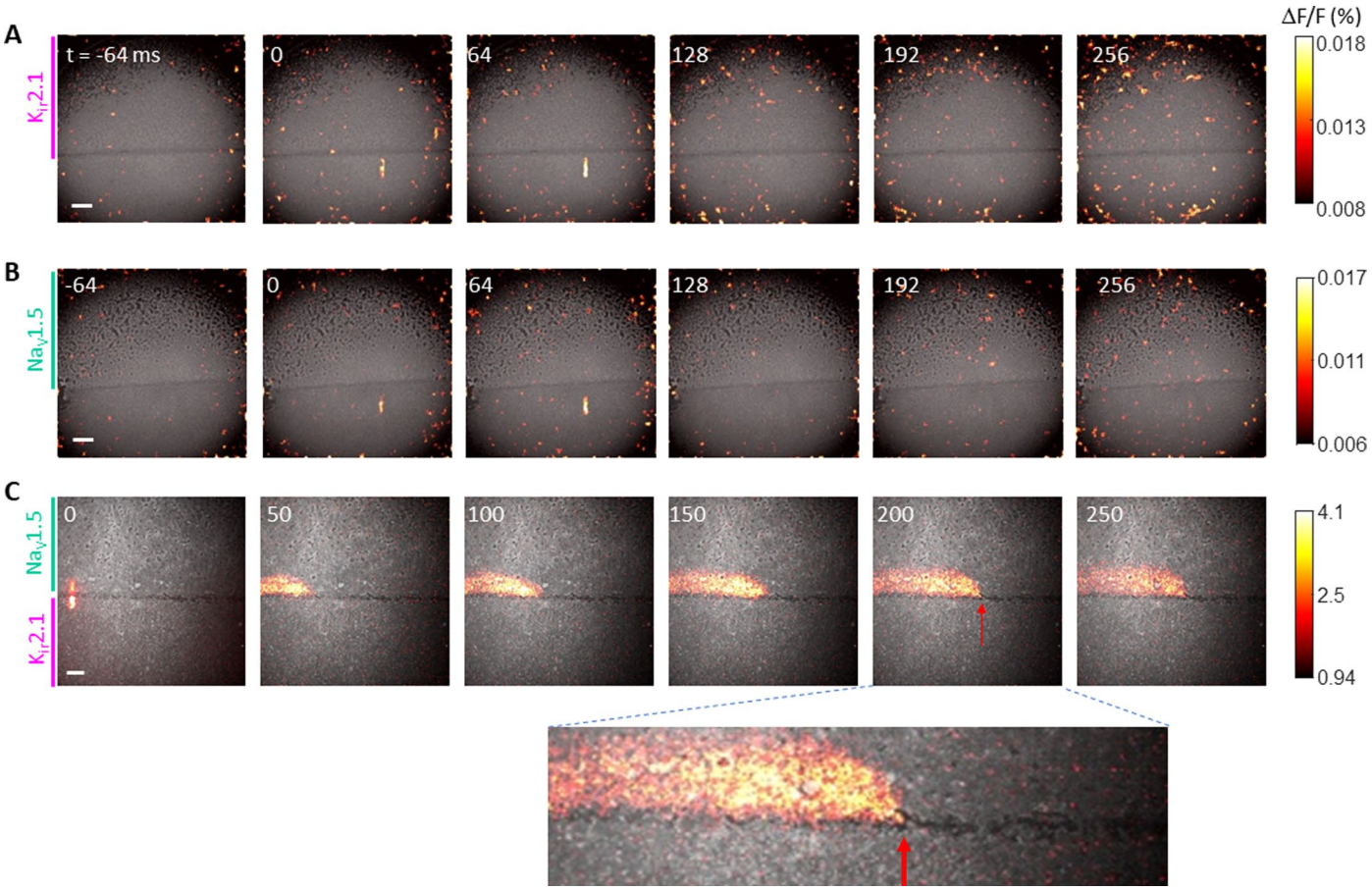

Extended Data Fig. 2 | Control experiments establishing necessary conditions for topological action potentials. a, b) Interfaces between populations of K_{ir}2.1- or Na_V1.5-expressing cells and cells not expressing either ion channel are not excitable. **c**) Topological AP propagation in a Na_V-K_{ir} interface was blocked in a region where cells did not migrate to fill the gap between the populations (red arrow). Scale bars 1 mm. Related to Fig. 1.

https://doi.org/10.1038/s41567-022-01853-z

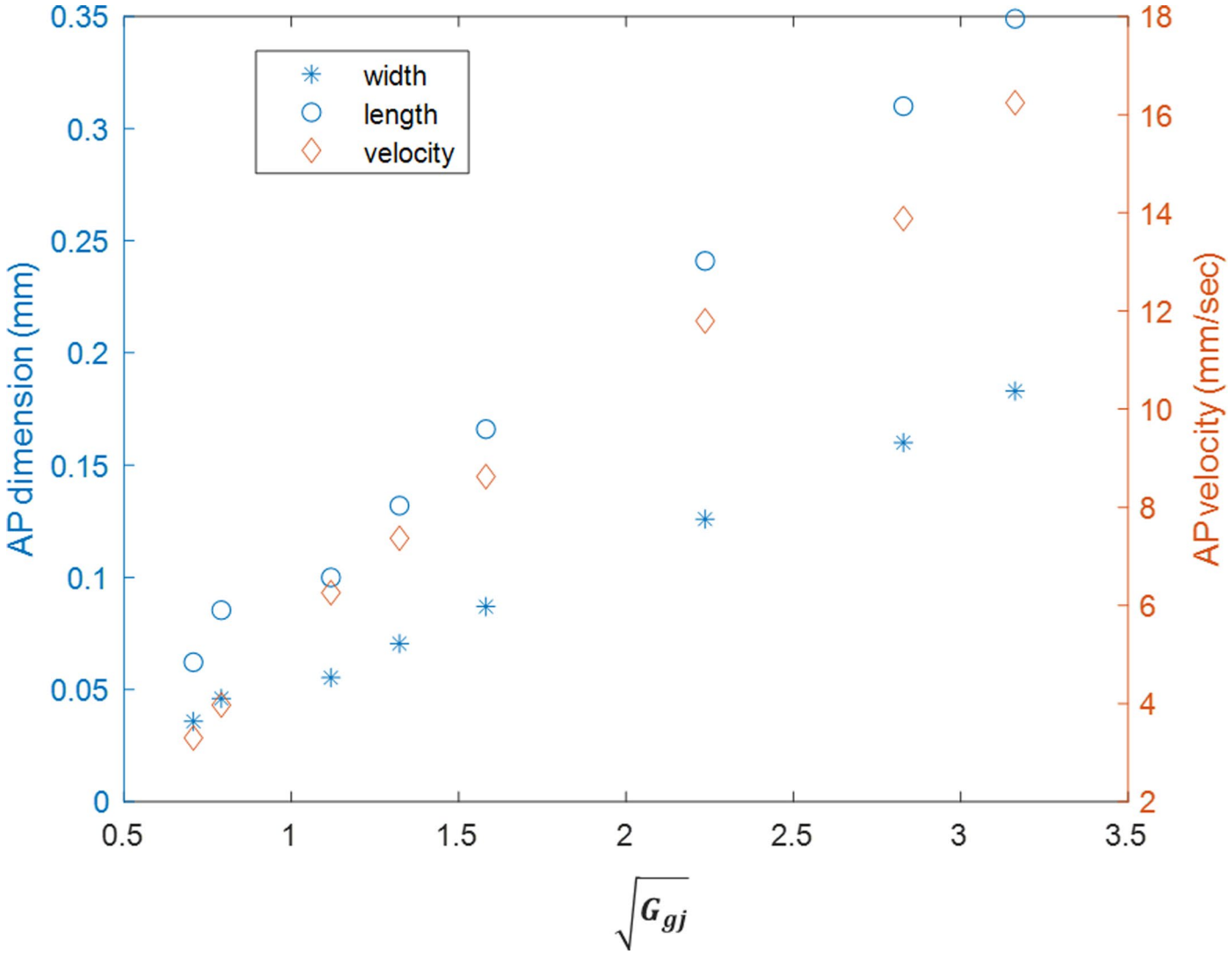

Extended Data Fig. 3 | Effect of gap junction conductance on topological action potential dimensions and velocity. The left y-axis corresponds to the simulated width and length of the topological AP, measured at half peak. The right y-axis corresponds to the AP velocity, extracted from AP kymographs[1]. As expected from dimensional analysis, all three quantities scale with $(G_{gj})^{\frac{1}{2}}$. Related to Fig. 2.

https://doi.org/10.1038/s41567-022-01853-z

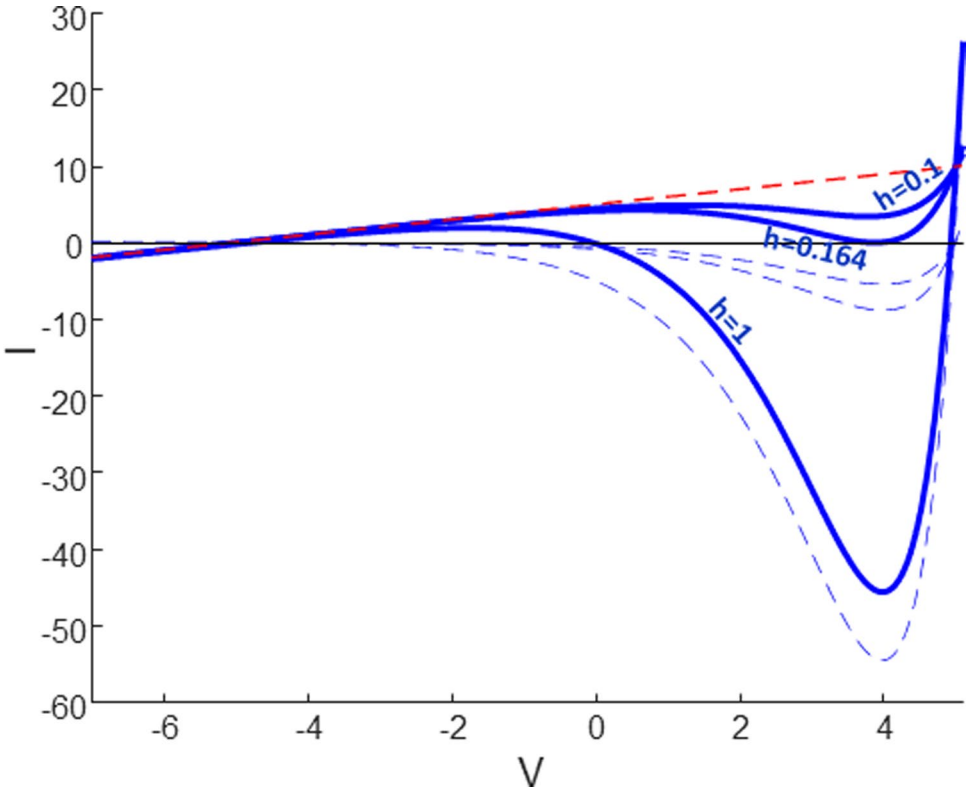

Extended Data Fig. 4 | I-V curves of a FHN- inspired model. I-V curves of cells with equal amounts of K_{ir} and Na_V and different values of h (solid lines); a 'K_{ir}-only' cell (red); and 'Na_V-only' cells with corresponding values of h (dashed blue). In this example, $A = 5$, $g_{Na} = g_K = 1$, and gap junctional currents are omitted. The upper fixed point disappears via a saddle-node bifurcation at $h \cong 0.164$. Related to Fig. 2.

https://doi.org/10.1038/s41567-022-01853-z

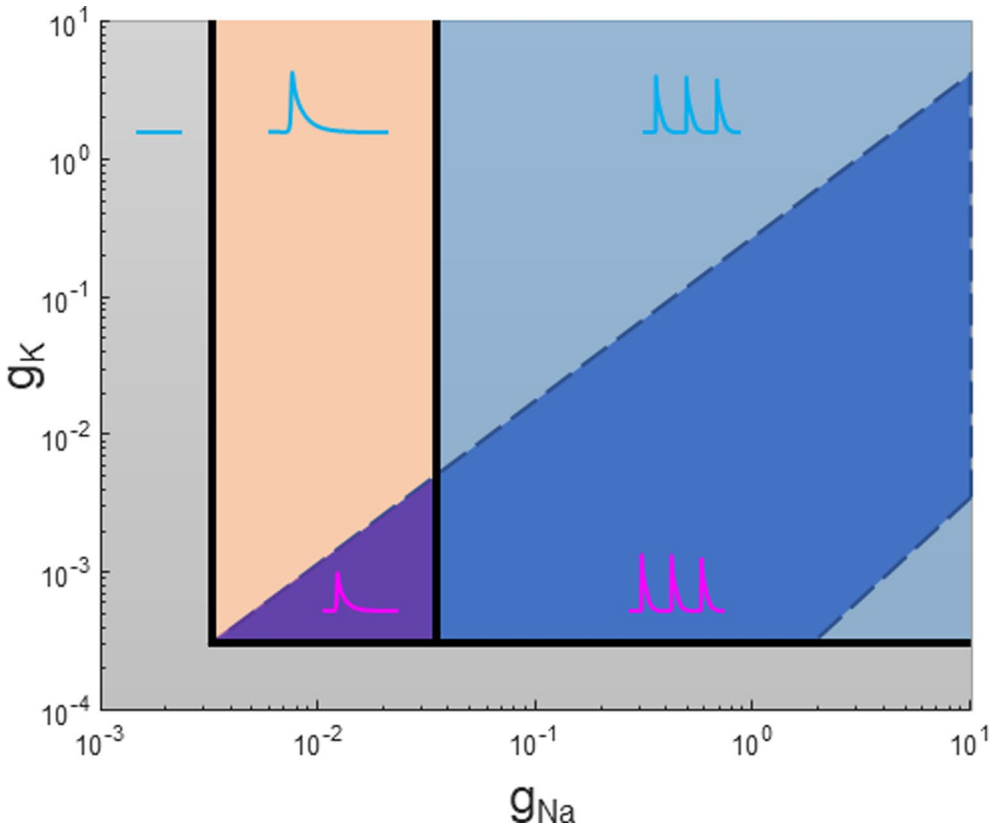

Extended Data Fig. 5 | Phase diagram of excitability of the FitzHugh-Nagumo-inspired model. The phase diagram is calculated both for the interface (background) and homogenous (shaded areas) configurations. The parameter space is divided into non-excitable, excitable, and spontaneously active phases. Like the realistic model (see Fig. 2c), the interface configuration shows little sensitivity to the values of g_K and g_{Na}. Other parameters: $\tau = 10^4; A = 5; B = 3; g_{stim} = 10^{-2}$. Related to Fig. 2.

https://doi.org/10.1038/s41567-022-01853-z

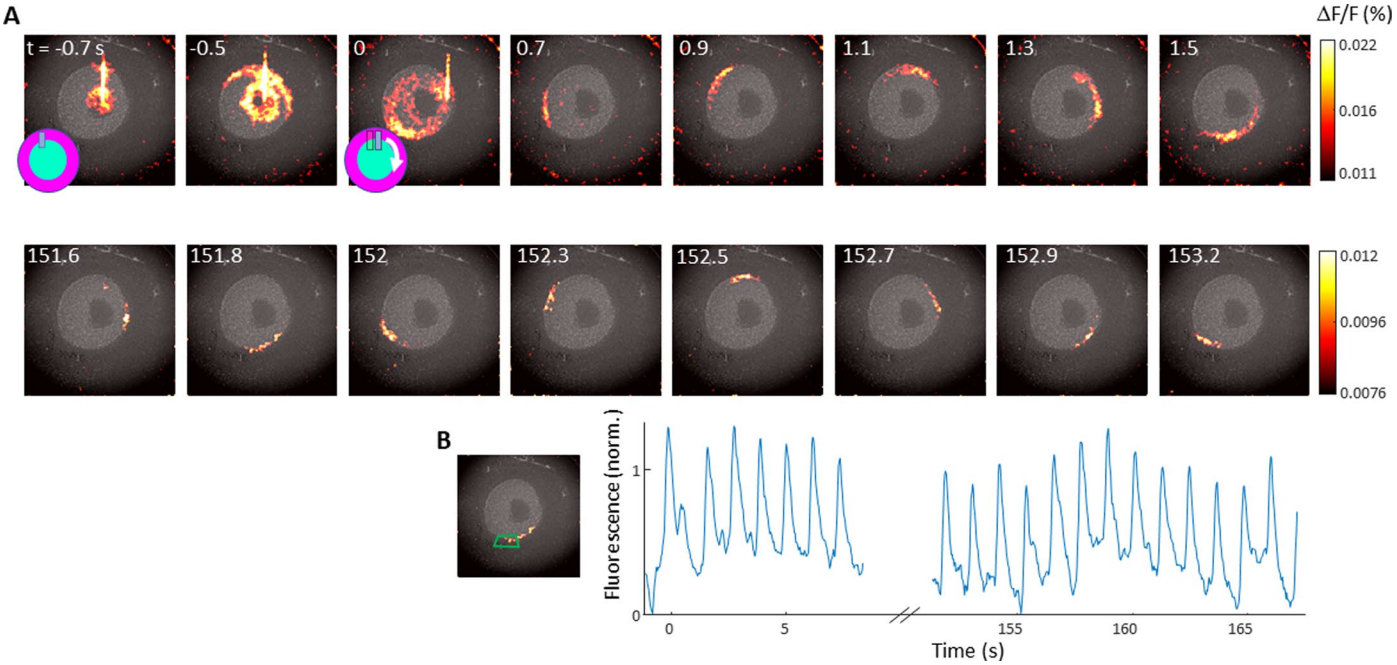

Extended Data Fig. 6 | Topological action potentials can propagate along a circular interface. a) Montage showing application of the inactivation stimulus, the trigger stimulus, and AP propagating for >150 s along the interface. **b**) Time-dependent fluorescence in the region indicated by the green polygon. Related to Fig. 3.

https://doi.org/10.1038/s41567-022-01853-z

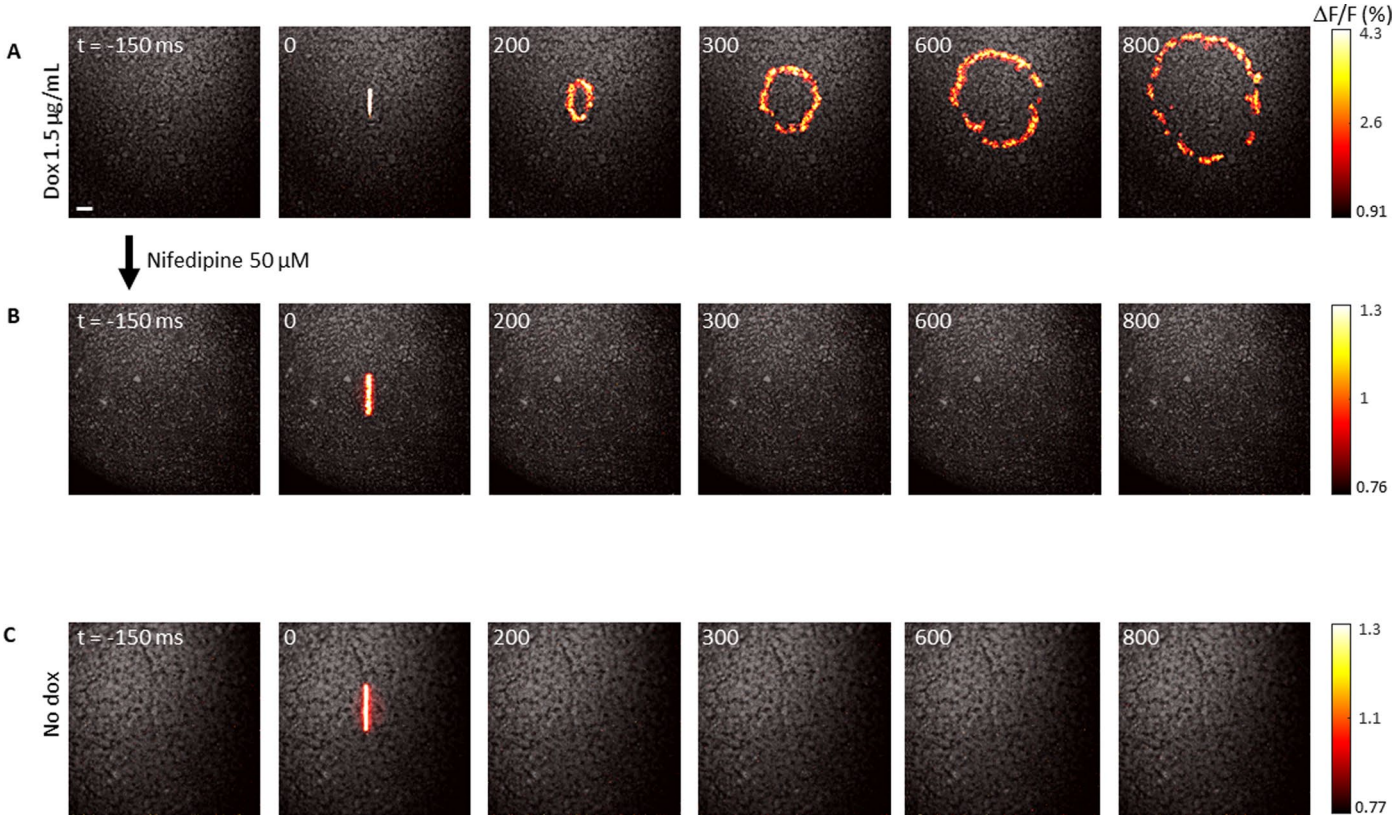

Extended Data Fig. 7 | Calcium-driven action potentials. Monolayers of HEK cells were grown expressing $Ca_V3.2$ (dox-induced), $K_{ir}2.3$ and CheRiff. **a**) After dox application (1.5 µg/mL for 1 day) to turn on $Ca_V3.2$ channel expression, the monolayer supported optically evoked action potential wave propagation. The thinner ring of active cells compared to Fig. 1b is attributable to the slower activation kinetics of $Ca_V3.2$ compared to $Na_V1.5$, leading to a slower wavefront velocity and hence a shorter wavelength. Scale bar: 1 mm. **b**) The $Ca_V3.2$ channel blocker nifedipine (50 µM) eliminated excitability of the cell monolayer. **c**) In the absence of doxycycline, the $Ca_V3.2$ channel was not expressed and the monolayer was not excitable. Related to Fig. 4.

nature physics

Article

https://doi.org/10.1038/s41567-022-01853-z

Observation of topological action potentials in engineered tissues

In the format provided by the authors and unedited

Supplementary Model 1: Hodgkin-Huxley-like model of interface APs

For realistic simulations of tissue interfaces, we used a Hodgkin-Huxley (HH)-like model, with the $Na_V1.5$ and $K_{ir}2.1$ currents separated along the x axis:

$$(1) \qquad C_m\dot{V} = G_{gj}\nabla^2 V - [I_{Na}H(x)+I_K H(-x)+I_{Leak}+I_{stim}(\mathbf{r},t)])$$

where $H(x)$ is the Heaviside step function:

$$(2) \qquad H(x) = \begin{cases} 0, & x \le 0 \\ 1, & x > 0 \end{cases}.$$

The simulation approach follows previous work from our lab.[1] I_{Na} represents a $Na_V1.5$ current, modeled using the Ten-Tusscher model.[2] The slow inactivation gate was set to j = 1, and the fast m gate was replaced by its asymptotic value $m_\infty(V)$:

$$\mathrm{I_{Na}} = g_{Na} m_\infty(V)^3 h(V,t)(V - E_{Na})$$

$$m_\infty(V) = \left(1 + e^{-\frac{56.86+V}{9.03}}\right)^{-2}$$

$$\dot{h} = \frac{h_\infty(V) - h}{\tau_h(V)}$$

$$h_\infty(V) = \left(1 + \mathrm{e}^{\frac{\mathrm{V}+71.55}{7.43}}\right)^{-2}$$

$$\tau_h(V) = \frac{1}{2}\left(1 - tanh\left(\frac{V+40}{10}\right)\right)\cdot\left(0.057\mathrm{e}^{-\frac{\mathrm{V}+80}{6.8}} + 2.7\mathrm{e}^{0.079\mathrm{V}} + 3.1\cdot 10^5 \mathrm{e}^{0.3485\mathrm{V}}\right)^{-1}$$

$$+\frac{1}{2}\left(1 + tanh\left(\frac{V+40}{10}\right)\right)\cdot\frac{1+\mathrm{e}^{-\frac{\mathrm{V}+10.66}{11.1}}}{5.92}.$$

Here $\tau_h(V)$ is a smoothed version of the original function in the Ten-Tusscher model, for numerical stability. The sodium reversal potential was set to E_{Na} = 75 mV.

I_K represents current through the inward-rectifying $K_{ir}2.1$ channel, modeled as an instantaneous function of voltage using the Ten-Tusscher model:[50]

$$I_K = g_K x_{K\infty}(V)(V - E_K)$$

$$x_{K\infty}(V) = 100\frac{\alpha_K(V)}{\alpha_K(V) + \beta_K(V)}$$

[1] McNamara, H. M. et al. Geometry-dependent arrhythmias in electrically excitable tissues. Cell Syst. 7, 359-370. e6 (2018).

[2] ten Tusscher, K. H. W. J., Noble, D., Noble, P. J. & Panfilov, A. V. A model for human ventricular tissue. Am. J. Physiol. - Heart Circ. Physiol. 286, H1573–H1589 (2004).

$$\alpha_K(V) = \frac{0.1}{1 + \mathrm{e}^{0.06(\mathrm{V}-\mathrm{E_K}-200)}}$$

$$\beta_K(V) = \frac{3\mathrm{e}^{\frac{\mathrm{V}-\mathrm{E_K}+100}{50000}} + \mathrm{e}^{\frac{\mathrm{V}-\mathrm{E_K}-10}{10}}}{1 + \mathrm{e}^{-\frac{\mathrm{V}-\mathrm{E_K}}{2}}}.$$

The potassium reversal potential was set to E_K = -107 mV.

The leakage term is an Ohmic conductance with reversal potential $E_{Leak} = 0$ mV:

$$I_{leak} = g_L V.$$

$I_{stim}(\mathbf{r}, t)$ is a stimulation term, $g_{ChR}(\mathbf{r}, t)V$, patterned in space and time to mimic optogenetic stimulation. The channelrhodopsin reversal potential was set to $E_{ChR} = 0$ mV.

All conductances were expressed in units of $\frac{nS}{pF}$, so $C_m = 1$. Spatial units were set to the spatial dimensions of a single cell, hence the gap-junction conductance G_{gj} had the same units as the ionic conductances. All voltages were expressed in mV and time in ms.

Simulations were performed in Matlab with a 300×300 grid of cells assigned to express either I_{Na} or I_K or both, depending on the configuration (homogeneous or interface) and the cell's location. Cell size and capacitance were set to 10 µm and 10 pF respectively. Gap-junction conductance was set to G_{gj} = 10 nS/pF. An Ohmic leak conductance, g_L = 0.005 nS/pF, was added to maintain stable resting potential in all cells. CheRiff stimulation was modeled as an additional Ohmic conductance with g_{ChR} = 0.5 nS/pF during periods of illumination. To calculate gap junctional currents, the Laplacian of the voltage was approximated by the discrete second-difference. No-flux boundary conditions were applied at the edges of the simulation. Euler's method was implemented for time integration with dt = 0.01 ms.

A 500 ms settling time was allowed at the beginning of each simulation, after which stimulus was delivered to the first 10 rows of cells for 10 ms. The excitability state of the simulated tissue (unexcitable, excitable or oscillating) was determined based on resting potential stability pre-stimulus and AP generation and propagation after stimulus. The parameter range for phase diagram construction was $[10^{-2},10^{2}]$ for g_K and $[10^{-1},10^{4}]$ for g_{Na}. Boundaries delineating the apparent phases were then drawn by interpolating between points near boundaries between dynamical regimes.

Supplementary Model 2: FitzHugh-Nagumo (FHN)-inspired model of interface APs

The purpose of the model presented hereafter in Equations (3) and (4) is to capture the key physics of excitable tissue interfaces in simplified equations which are more analytically tractable than the Hodgkin-Huxley (HH)-like model presented above.

To design a simplified model, we adapted the FitzHugh-Nagumo (FHN) model[37,38] of neuronal excitability. In the FHN model, excitability is manifested as an 'N' shaped I-V curve (or $\dot{V}$-V curve) at rest, with 2 stable fixed points. Starting at the lower (more polarized) fixed point, a depolarizing stimulus engages positive feedback which drives the system to the upper fixed point. A slower variable then starts shifting the I-V curve, until eventually, at a critical lower value, the upper fixed point disappears via a saddle-node bifurcation, forcing the system to repolarize and return to the lower fixed point.

To allow spatial segregation of the depolarizing and hyperpolarizing currents, we replace the cubic polynomial of the original FHN model by a combination of two terms, corresponding to the Na^+ and K^+ currents. Only when these two currents are added together does the I-V curve acquire the desired 'N' shape (Fig. S4). The non-linear Na^+ current by itself has only one fixed point, but when it is tilted by the added linear K^+ current another stable fix point appears in the hyperpolarized regime.

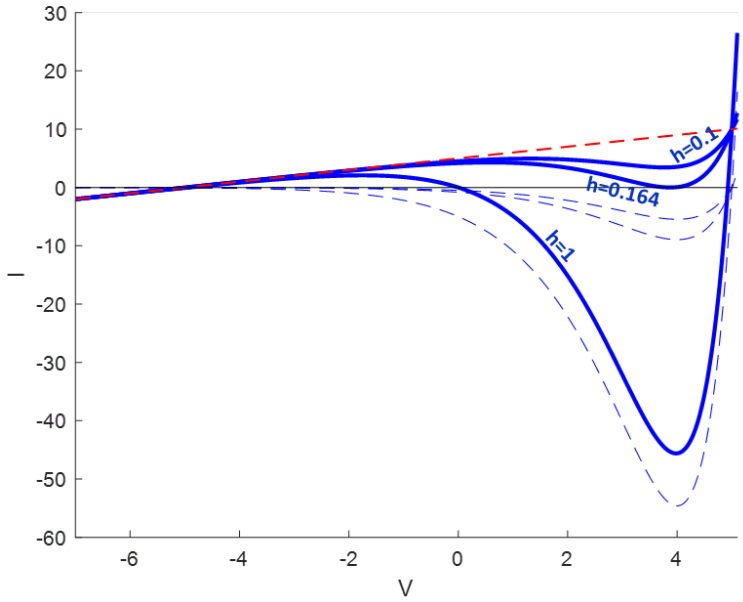

Figure S4. I-V curves of a FHN- inspired model. I-V curves of cells with equal amounts of K_{ir} and Na_V and different values of h (solid lines); a "K_{ir}-only" cell (red); and "Na_V-only" cells with corresponding values of h (dashed blue). In this example, A = 5, $g_{Na} = g_K = 1$, and gap junctional currents are omitted. The upper fixed point disappears via a saddle-node bifurcation at $h \cong 0.164$. Related to Fig. 2.

Next, the Na^+ and K^+ currents are spatially segregated, as in the HH-like model (see Supplementary Model 1):

(3) $$\dot{V} = \nabla^2 V - H(x) g_{Na} e^V (V - A) h(V,t) - H(-x) g_K (V + A) - g_{stim}(\mathbf{r}, t) \cdot V$$

(4) $$\tau \dot{h} = -V - B - h,$$

Here we express the conductances g_{Na} and g_K as unitless entities, representing ratios to the gap-junction conductance, which we set to 1.

Following the development of the FHN model, a slow variable h is introduced. Here it corresponds to the inactivation gate of the sodium channel, and therefore the h variable scales the sodium current term. When h decreases the curve flattens towards the linear K^+ current, until the upper fixed point disappears at $h = -\frac{g_K}{g_{Na}} \frac{e^{-\sqrt{A(A-2)}}}{\sqrt{A(A-2)} - A + 1}$.

In contrast to the FHN model, in our model the current term ($\dot{V}$) retains the overall structure of the HH model, $\dot{V} = \nabla^2 V - \sum_i g_i(x) f_i(V,t)(V - E_i)$. Therefore, its parameters retain, at least approximately, a biophysical interpretation. In Eq.(1), the second term on the r.h.s. corresponds to a Na_V-like current, and the third term corresponds to a K_{ir}-like current, though these terms no longer match specific ion channels.

As a technical note, to obtain an 'N' shaped *I-V* curve, the nonlinearity only needs to be incorporated in one ionic current. Therefore, in our minimal model the K_{ir}-like current is ohmic-like (linear).

This simple model shows topological APs similar to those observed experimentally (Fig. 2E), with the closest approximation obtained with the following parameters: $g_{Na} = 10^{-2}, g_K = 10^{-3}, \tau = 10^4, A = 5, B = 3$. The phase diagram of excitability of the FHN-like model reproduce the main features of the realistic model (Fig. S5; compare to Fig. 2C): excitability of the interface

configuration was not sensitive to the value of g_K. Increasing g_{Na} shifted the system from stimulus-triggered excitability to spontaneous oscillations. Excitability of the homogenous system was sensitive to g_K and g_{Na}. Unlike in the realistic model, in the FHN-like model the homogenous system includes an oscillatory phase, due to the range of allowed h values, which in this model extends to negative values.

Simulations were carried with dt = 0.1 time units. For each instantiation, the system was allowed to settle with $h = h_\infty = -V - B$ for 5000 time units, after which 1000-3000 time units of a full run were tested for spontaneous oscillations. Then a stimulus was delivered for 100 time units after which the system was tested for stimulus evoked excitability. The parameter range was $[10^{-4},10^{2}]$ for both g_K and g_{Na}.

Supplementary Code

%% Matlab code for simulating FHN-like model of topological APs

```
% Model equations:
% dV/dt = Laplacian(V) - gNa*exp(V)*(V-A)*h - gK*exp(-V)*(V+A) - gStim*V
% dh/dt = (-V-B-h)/tau
% Here V, h, are functions of space and time, dependent variables.
% gNa, gK, are functions of space, independent variables.
% gStim is a function of space and time, independent variable.
% A, B, tau are constants.

% define model parameters
gNa = 1e-2;
gK = 1e-3;
gStim = 1;
tau = 1e4;
A = 5;
B = 3;

% define grid dimensions
nx = 300;
ny = 300;

% define which cells express Kir-like conductance
KirCells = zeros(ny, nx);
KirCells(1:ny/2,:)=1;

% define which cells express NaV-like conductance
NaVCells = zeros(ny, nx);
NaVCells(ny/2+1:end, :)=1;

% define which cells will be stimulated
stimCells = zeros(ny, nx);
stimCells(:, 10:20) = 1;


% define voltage initial conditions
V = zeros(ny, nx);
V(logical(NaVCells)) = -B;
V(logical(KirCells)) = -A;

% define h to take its asymptotic value
h = -V-B;

% configure simulation parameters
t_init = 3000;  % time to run to reach initial steady-state.
t_stim = t_init + 300;  % start the stimulus 300 time units after main
simulation starts
t_end = t_stim + 10000;  % run the simulation for 1e4 time-steps after stim
starts.
stim_dur = 100;

dt = .1;
downsamp = 100;  % how much to downsample the stored dynamics in time
```

```
% prepare stimulation timing. One stimulus
stim = zeros(t_end/dt, 1);
stim (t_stim/dt:(t_stim+stim_dur)/dt) = 1;

% initialize variables to store V and h
V_traces = zeros(ny, nx, t_end/downsamp);
h_traces = zeros(ny, nx, t_end/downsamp);


figure
%initialization run. Assumes dh/dt=0  ==> h = -V-B;
for i = 1:t_init/dt

    % calculate Laplacian(V)
    V_aux = zeros(ny + 2, nx + 2);
    V_aux(2:end-1, 2:end-1) = V;
    V_aux(1, :) = V_aux(2,:);
    V_aux(end, :) = V_aux(end-1, :);
    V_aux(:, 1) = V_aux(:, 2);
    V_aux(:, end) = V_aux(:, end-1);

    delV = (V_aux(1:end-2, 2:end-1) + V_aux(3:end, 2:end-1) + V_aux(2:end-1,
1:end-2) + V_aux(2:end-1, 3:end))./4 - V;

    %calculate dv/dt and update V, assuming dh/dt=0
    h = -V-B;
    dvdt = delV - NaVCells.*gNa.*exp(V).*(V-A).*h - KirCells.*gK.*(V+A) -
stimCells.*gStim.*stim(i).*V;
    V = V + dvdt.*dt;
    %update display and store V and h values every 100 time points
    if mod(i,downsamp/dt) == 0
        t = i/(downsamp/dt);

        disp(t)

        imagesc(V,[-A,A])

        title (['initialization ',num2str(t*downsamp-t_init)])

        drawnow
        index = round(t);
        V_traces(:,:,index) = V;
        h_traces(:,:,index) = h;

    end
end

%now the actual simulation, with full dynamics of h
for i = t_init/dt+1:t_end/dt
    % calculate Laplacian(V)

    V_aux = zeros(ny + 2, nx + 2);
    V_aux(2:end-1,2:end-1) = V;
```

```
    V_aux(1,:) = V_aux(2,:);
    V_aux(end, :) = V_aux(end-1, :);
    V_aux(:, 1) = V_aux(:, 2);
    V_aux(:, end) = V_aux(:, end-1);

    delV = (V_aux(1:end-2, 2:end-1) + V_aux(3:end, 2:end-1) + V_aux(2:end-1,
1:end-2) + V_aux(2:end-1, 3:end))./4 - V;

    %calculate dv/dt
    dvdt = delV - NaVCells.*gNa.*exp(V).*(V-A).*h - KirCells.*gK.*(V+A) -
stimCells.*gStim.*stim(i).*V;

    %     calculate dh/dt
    dhdt = (-V-B-h)./tau;

    %  update V and h
    V = V + dvdt.*dt;
    h = h + dhdt.*dt;
    %update display and store V and h values every 100 time points
    if mod(i,downsamp/dt) == 0
        t = i/(downsamp/dt);

        disp(t)

        imagesc(V,[-A,A])

        title (num2str(t*downsamp - t_stim))

        drawnow
        index = round(t);
        V_traces(:,:,index) = V;
        h_traces(:,:,index) = h;

    end
end
```

nature portfolio

Corresponding author(s): Adam Cohen

Last updated by author(s): Jun 7, 2022

Reporting Summary

Nature Portfolio wishes to improve the reproducibility of the work that we publish. This form provides structure for consistency and transparency in reporting. For further information on Nature Portfolio policies, see our Editorial Policies and the Editorial Policy Checklist.

Statistics

For all statistical analyses, confirm that the following items are present in the figure legend, table legend, main text, or Methods section.

n/a	Confirmed
☐	☒ The exact sample size (*n*) for each experimental group/condition, given as a discrete number and unit of measurement
☐	☒ A statement on whether measurements were taken from distinct samples or whether the same sample was measured repeatedly
☒	☐ The statistical test(s) used AND whether they are one- or two-sided *Only common tests should be described solely by name; describe more complex techniques in the Methods section.*
☒	☐ A description of all covariates tested
☒	☐ A description of any assumptions or corrections, such as tests of normality and adjustment for multiple comparisons
☐	☒ A full description of the statistical parameters including central tendency (e.g. means) or other basic estimates (e.g. regression coefficient) AND variation (e.g. standard deviation) or associated estimates of uncertainty (e.g. confidence intervals)
☒	☐ For null hypothesis testing, the test statistic (e.g. *F*, *t*, *r*) with confidence intervals, effect sizes, degrees of freedom and *P* value noted *Give P values as exact values whenever suitable.*
☒	☐ For Bayesian analysis, information on the choice of priors and Markov chain Monte Carlo settings
☒	☐ For hierarchical and complex designs, identification of the appropriate level for tests and full reporting of outcomes
☒	☐ Estimates of effect sizes (e.g. Cohen's *d*, Pearson's *r*), indicating how they were calculated

Our web collection on statistics for biologists contains articles on many of the points above.

Software and code

Policy information about availability of computer code

Data collection	All data were acquired using custom-built instrumentation controlled via National Instruments Data Aquisition Systems (DAQ) and custom MATLAB (R2018b) software.
Data analysis	All data were processed and analyzed using custom MATLAB (R2018b) software.

For manuscripts utilizing custom algorithms or software that are central to the research but not yet described in published literature, software must be made available to editors and reviewers. We strongly encourage code deposition in a community repository (e.g. GitHub). See the Nature Portfolio guidelines for submitting code & software for further information.

Data

Policy information about availability of data

All manuscripts must include a data availability statement. This statement should provide the following information, where applicable:

- Accession codes, unique identifiers, or web links for publicly available datasets
- A description of any restrictions on data availability
- For clinical datasets or third party data, please ensure that the statement adheres to our policy

Data are available from the authors upon reasonable request.

Human research participants

Policy information about studies involving human research participants and Sex and Gender in Research.

Reporting on sex and gender	*Use the terms sex (biological attribute) and gender (shaped by social and cultural circumstances) carefully in order to avoid confusing both terms. Indicate if findings apply to only one sex or gender; describe whether sex and gender were considered in study design whether sex and/or gender was determined based on self-reporting or assigned and methods used. Provide in the source data disaggregated sex and gender data where this information has been collected, and consent has been obtained for sharing of individual-level data; provide overall numbers in this Reporting Summary. Please state if this information has not been collected. Report sex- and gender-based analyses where performed, justify reasons for lack of sex- and gender-based analysis.*
Population characteristics	*Describe the covariate-relevant population characteristics of the human research participants (e.g. age, genotypic information, past and current diagnosis and treatment categories). If you filled out the behavioural & social sciences study design questions and have nothing to add here, write "See above."*
Recruitment	*Describe how participants were recruited. Outline any potential self-selection bias or other biases that may be present and how these are likely to impact results.*
Ethics oversight	*Identify the organization(s) that approved the study protocol.*

Note that full information on the approval of the study protocol must also be provided in the manuscript.

Field-specific reporting

Please select the one below that is the best fit for your research. If you are not sure, read the appropriate sections before making your selection.

☒ Life sciences ☐ Behavioural & social sciences ☐ Ecological, evolutionary & environmental sciences

For a reference copy of the document with all sections, see nature.com/documents/nr-reporting-summary-flat.pdf

Life sciences study design

All studies must disclose on these points even when the disclosure is negative.

Sample size	The main observation of the study (topological action potential along a linear interface, fig 1E) was observed on 5 independent samples. All other the observations were performed in 2 or more independent samples.
Data exclusions	No data were excluded from the study.
Replication	All qualitative findings were replicated in at least one separately prepared biological replicate
Randomization	Randomization was not used.
Blinding	Investigators were not blinded.

Reporting for specific materials, systems and methods

We require information from authors about some types of materials, experimental systems and methods used in many studies. Here, indicate whether each material, system or method listed is relevant to your study. If you are not sure if a list item applies to your research, read the appropriate section before selecting a response.

Materials & experimental systems

n/a	Involved in the study
☒	☐ Antibodies
☐	☒ Eukaryotic cell lines
☒	☐ Palaeontology and archaeology
☒	☐ Animals and other organisms
☒	☐ Clinical data
☒	☐ Dual use research of concern

Methods

n/a	Involved in the study
☒	☐ ChIP-seq
☒	☐ Flow cytometry
☒	☐ MRI-based neuroimaging

Eukaryotic cell lines

Policy information about cell lines and Sex and Gender in Research

Cell line source(s)	HEK 293T cells were purchased from ATCC.
Authentication	HEK 293T cells were not independently validated after purchase from ATCC.
Mycoplasma contamination	All cell lines used tested negative for mycoplasma contamination.
Commonly misidentified lines (See ICLAC register)	N/A